

MIPS/SED Mode: Data Details and Calibration (for the MIPS handbook)

Nanyao Lu¹ for MIPS IST/IT

Contents

1	INTRODUCTION TO THE MIPS SED MODE	2
2	BCD DATA	2
3	POST-BCD DATA	5
3.1	Pipeline Mosaics and Default Spectrum Extraction	5
3.2	Making Your Own Mosaics	5
4	CALIBRATION OF THE MID/SED MODE	7
4.1	Overview	7
4.2	Illumination Correction	7
4.3	Wavelength Calibration	12
4.4	Aperture Correction	12
4.5	Flux Calibrations	15
4.5.1	Calibration Stars and Spectral Response Function	15
4.5.2	Comparison with Models and Previous Observations	17
4.5.3	Pointing Offsets and Flux Systematics in some Campaigns	26
4.5.4	Extended Source Fluxes	26
4.5.5	Remarks on Flux Nonlinearity	28

1. INTRODUCTION TO THE MIPS SED MODE

The Spectral Energy Distribution (SED) mode of MIPS provides a capability of obtaining long-slit, low-resolution ($R \approx 15\text{-}25$) spectra in the far infrared ($52\text{-}97\ \mu\text{m}$). The SED slit is two detector pixels ($\sim 20''$) in width, and 12 pixels ($\sim 2'$) in length where the full wavelength coverage is available. An inoperative detector module restricts the wavelength coverage to only $65\text{-}97\ \mu\text{m}$ over the last 4 columns of the 16×32 detector array.

A standard SED observation provides pairs of data frames between the target position (ON) and a nearby sky position (OFF). The scan mirror is used to chop between the ON and OFF, and an observer can choose a chop throw of $+3'$, $+2'$, $+1'$, or $-1'$. The observer can request either a pointed observation or an $M\times N$ raster map (with M, N between 1 and 100). For a pointed observation (or at each raster position in the case of a raster map), there is a basic set of 6 pairs of ON and OFF frames (plus bracketing frames on the internal stimulator (for tracking detector responsivity variations), of which the first 3 pairs are obtained with the target placed near the center of detector column 10 (hereafter referred to as dither position 1) and the next 3 pairs with the target near the center of column 5 (dither position 2). The observer repeats this basic observing set by a number of cycles (N_c) in order to reach the desired S/N ratio. For a mapping observation, the value of N_c remains the same for all the raster positions.

Using the same detector and internal stimulators, the SED mode shares some calibration characteristics (e.g., dark current) with the $70\ \mu\text{m}$ imaging mode. As a result, most of the discussion on the data products and detector calibration (e.g., , dark current) of the default $70\ \mu\text{m}$ imaging mode in the previous chapters applies directly to the SED mode. In this chapter, we describe in some detail the data products at BCD (§2) and post-BCD (§3) levels and the instrumental calibration (§4) that are specific to the SED mode.

2. BCD DATA

BCD images have been fully corrected for all basic instrumental effects. The file names of the SED BCD products follow the same convention as the $70\ \mu\text{m}$ image mode (cf. Table 3.3). However, for the SED mode, one should use only the unfiltered BCD images for further analysis or mosaicking.

Each BCD flux image is a FITS file with the dispersion axis along the vertical Y-axis. The blue end of the spectrum is at the bottom of the image. The pixel size along the (horizontal) spatial axis is $9.80''$ (CDELTA1). The dispersion solution is given by the header keywords CRVAL2, CRPIX2 and CDELTA2, which lead to a dispersion scale of $1.71\ \mu\text{m}/\text{pixel}$

and the first detector row corresponding to $52.55\ \mu\text{m}$ (see §4.3 for more details on the wavelength calibration). The effective wavelength coverage is $51.7\text{--}97.8\ \mu\text{m}$ over detector rows 1–27. The final 5 detector rows are contaminated by second-order diffracted light, and are not calibrated. Consequently, these rows have been masked out. An inoperative detector module restricts the wavelength coverage to only $65\text{--}97\ \mu\text{m}$ over the last 4 columns of the 16×32 detector array. The astrometry of each BCD image is given by the header keywords RA_SLT, DEC_SLT and the slit orientation on the sky (PA_SLT, which is defined to be from North to the BCD image positive X-axis in a counter-clock way). One way to identify stim exposures is look for the BCD files with a non-zero value for the header keyword STMFL_70.

Fig. 1 illustrates two typical BCD images taken respectively at the two dither positions of the SED mode. Note that, as mentioned in §1, the target is placed near the centers of the detector columns 10 and 5 at dither positions 1 and 2, respectively.

The SED flux calibration is based on a subset of calibration stars with a pre-determined far-infrared spectrum (see §4.5 for more details). The flux scale of a BCD image is in units of MJy sr^{-1} . This is derived from the calibration star observations as follows:

$$\text{flux scale} = f_{\nu}(\lambda_c)/\Sigma/A, \quad (1)$$

where $f_{\nu}(\lambda_c)$ is the stellar flux density at the central wavelength λ_c of the detector pixel under consideration, Σ is the MIPS number counts within an aperture of 5 detector columns centered at the calibration star, and A is the angular size of each detector pixel, which is assumed to be a square of $9.8'' \times 9.8''$. As a result, one arrives at a *true* point-source flux density in Jansky by (i) adding together the BCD pixel values over a 5-detector column aperture centered on the target and then (ii) multiplying the sum by A .

For a spectrum of an extended source or a point source extracted with an aperture other than the default one of 5 detector columns, correct fluxes can be derived using the aperture correction factors in Table 4.4 in §4.4.

One should also be aware of the fact that the flux scale is calibrated using the sky-subtracted, mosaicked images (see §3 of the observed calibration stars (see §4.5 for more details on flux calibration). There could be a small systematic flux difference between the two dither positions at the BCD level due to a residual illumination correction issue (see §4.2). It is therefore advised that one should always use the mosaicked image for formal photometry on point sources.

There are a number of remaining issues at the BCD level, including a small spectral tilt of about 1° (given by the BCD header keyword CROTA2) and some small array distortion. Corrections for these issues are addressed in the post-BCD data process (see §3).

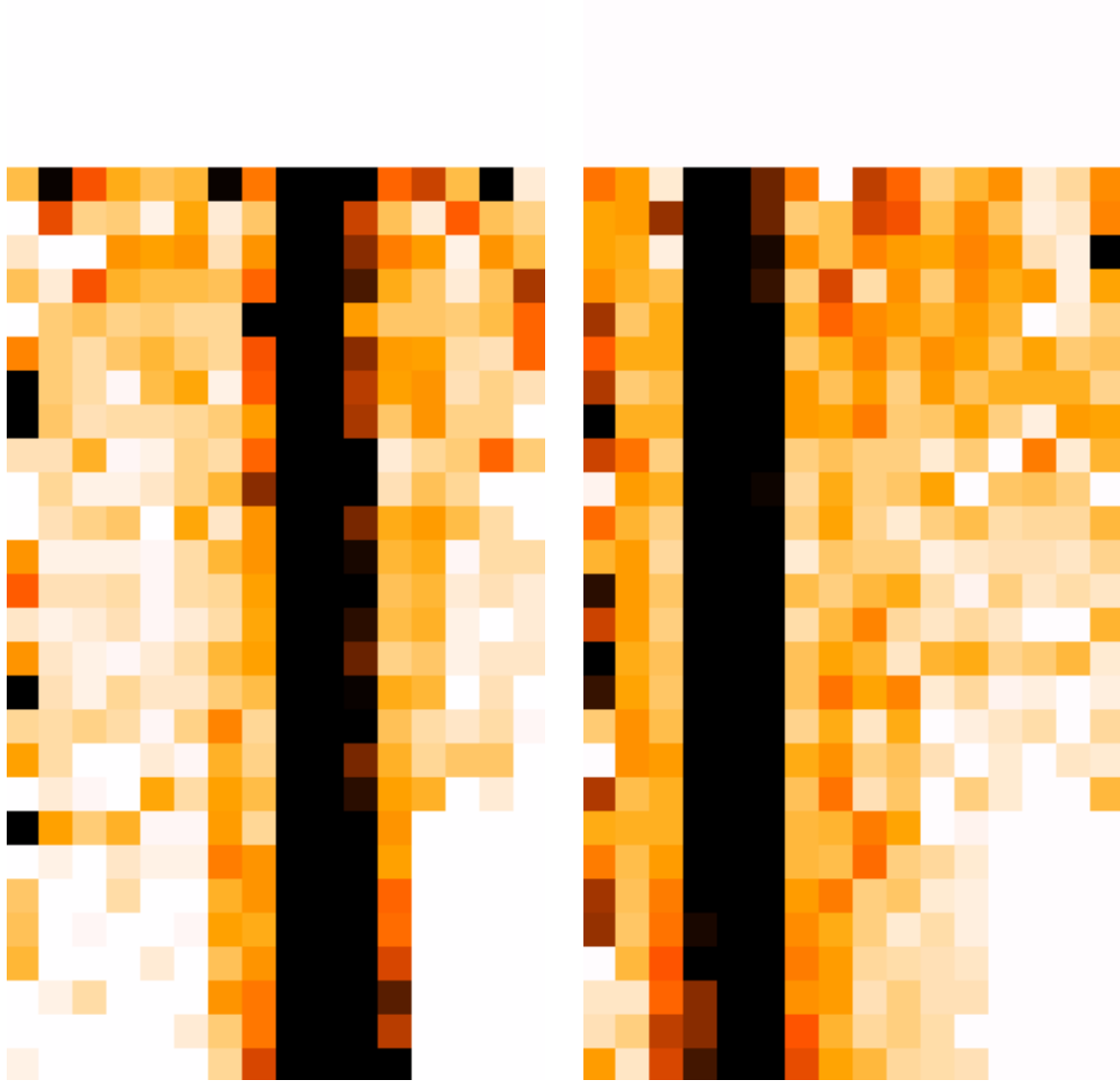


Fig. 1.— BCD images from an observation of the star HD 108903, showing the spectral locations on the detector array. The left panel is take at dither position 1 while the right panel at dither position 2. Note that the dead module is at the left bottom corner in each image and that only detector rows 1-27 are properly calibrated.

3. POST-BCD DATA

3.1. Pipeline Mosaics and Default Spectrum Extraction

The post-BCD pipeline data processing fulfills the following requirements: (1) correction for a small spectrum tilt and perform distortion corrections, (2) derive mosaic images for ON, OFF and ON-OFF using the actual pointing information, and (3) a default extraction of a 1-d spectrum from the ON-OFF mosaic.

The basic algorithm of the post-BCD pipeline processing of the SED data is described in a MOPEX document on "mosaic_sed.pl," available at the SSC data reduction website. It uses the standard area-weighted interpolation in mosaicking. For a pointed observation (or each raster point in a raster map), two mosaics are generated, one for each of the ON and OFF pointings. A difference mosaic between the ON and OFF mosaics is also derived, from which a sky-subtracted spectrum is extracted by placing a 5-column aperture centered in the column with the largest flux sum between detector rows 2 and 20. Table 2 lists some important post-BCD files for the SED mode.

The plain text file "..._sed.tbl" (e.g., SPITZER_M2_17169162_1_A9183226_sed.tbl) follows IPAC table format with a short header showing the position of the target (RA_SOURCE and DEC_SOURCE), the actual columns (i.e., COLUMN_1 to COLUMN_5) in the mosaic for the spectrum extraction, etc. The table itself contains 5 columns, which are (1) detector row number, (2) wavelength in microns, (3) flux density in Jy, (4) flux density uncertainty in Jy, and (5) the aperture correction factor used in deriving columns (3) and (4). Fig. 2 illustrates such a post-BCD spectrum from an observation of star HD 45348 along with a model-predicted spectrum.

It should be pointed out that the default pipeline spectrum extraction is for your inspection only. You may well need to do your own spectral extraction using the ON-OFF mosaic image.

3.2. Making Your Own Mosaics

You also have the option of making your own mosaics with the offline SED mosaicking tool "mosaic_sed.pl" which is equivalent to the post-BCD pipeline if you use the same values for the controlling parameters as the pipeline. The tool is a part of the MOPEX package and is downloadable from the SSC website.

There may have some advantages to do your own mosaics. For example, you can do

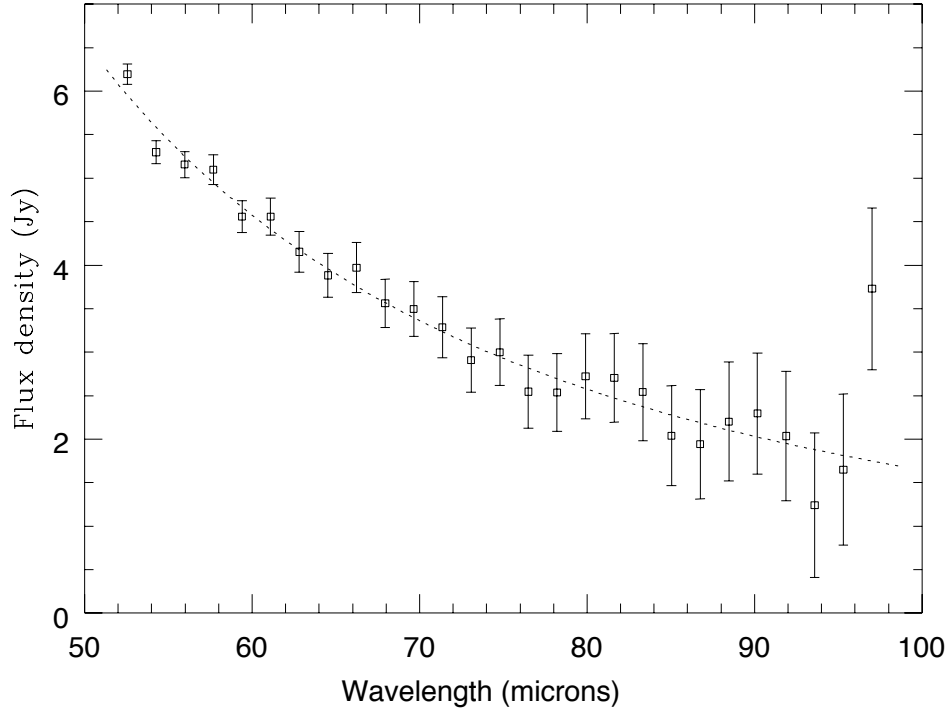


Fig. 2.— Plot of the post-BCD extracted spectrum (squares) from an observation of the star HD 45348 in MC21 in comparison with a model predicted spectrum (dotted line).

further data manipulation at the BCD level before mosaicking; you can also use a different interpolation option than the default one. If you have a raster map you can use this offline tool to produce a big mosaic using all the raster points.

The program uses a NameList file as an input. In the file you specify lists of image to process and where the results should be output. The instructions on this NameList file as well as how to set up and run this program are given in the user’s manual of ”mosaic_sed.pl,” also available at the SSC website.

4. CALIBRATION OF THE MID/SED MODE

4.1. Overview

The steps of calibrating the MIPS/SED mode are similar to that of the MIPS $70\mu\text{m}$ imaging mode, including (a) cosmic ray identification and rejection, (b) corrections for latency effects and other non-linearities, (c) pixel response correction using stim flashes, (d) dark correction, (e) illumination correction (i.e., flat fielding), (f) wavelength calibration, (g) aperture correction, and (h) flux calibration. Steps (a)-(d) are the same as in the imaging mode, which have been discussed in the previous chapter. We describe briefly here steps (e)-(h), for which the SED mode differs in some way from the imaging mode. For general procedures on the MIPS Ge calibration, see Gordon et al. (2005, 2006).

As of S15(?) the flux calibration is based on multiple observations of 3 bright stars (HD108903, HD124897, and HD029139) with $70\mu\text{m}$ flux densities of 13-19 Jy. The point-source flux calibration accuracy is estimated to be 10% or better down to at least 0.5 Jy at the blue end of the spectrum and to ~ 2 Jy near the red end, based on SED observations of fainter standard stars and comparison with independent data from other instruments. With additional uncertainties from the illumination and aperture corrections included, the surface brightness calibration of extended sources is accurate to $\sim 15\%$. The flux repeatability in time is better than 5%. A full description of the MIPS SED calibration will be given elsewhere (Lu et al. 2006).

4.2. Illumination Correction

The characterization of the combined effect of a non-uniform illumination pattern and the difference in illumination between sky and the internal, undispersed stimulator flashes can be calibrated by imaging celestial sources of uniform surface brightness (see Gordon

et al. 2005). We have utilized SED observations of diffuse Galactic emission (with *IRAS* $I_\nu(60\mu\text{m})/I_\nu(100\mu\text{m}) \sim 0.2 - 0.3$) near the Galactic plane. Once an adequate number of independent observations have been acquired, a median filtering is performed to filter out any spatial structure that might be present in individual observations. To reach a good signal level (i.e., 5-10 times the level of the dark current), we targeted regions where *IRAS* $I_\nu(60\mu\text{m}) = 200 - 300\text{MJy sr}^{-1}$ and where no *IRAS* point sources are identified within a radius of about 5'-10'. Each of the selected regions is observed in a 4x1 map with a chop throw of 2'. Fig. 3 compares the individual IC observations by plotting their normalized mean spatial profiles, together with their median result.

Fig. 3 also shows that the instrumental sensitivity drops substantially for the first couple of detector columns. A possible explanation could be that the end of the slit vignettes these detector columns. The first detector column also shows a much greater pixel-to-pixel noise level compared with the other detector columns. It is therefore recommended that this entire column, although included in the data reduction and calibration steps, be ignored in any science analysis.

The current IC approach is quite efficient, reaching good signal levels over the entire detector array using a reasonable amount of telescope time. However, we found some residual systematic variation of up to $\sim 15\%$ along the spatial axis of the slit. This effect is illustrated in Fig. 4 using the data from a 16x1 mapping observation of the point source-like galaxy Arp 231. The target was scanned along the slit with a step size matching the detector pixel size. For each raster pointing, the on-target frames from one of the two default dither positions have been coadded and sky subtracted, and a 3-column aperture was used to extract a spectrum. The results from all the 16 pointings are shown in Fig. 4 for two detector row ranges.

Fig. 4 reveals two important characteristics: (1) Excluding the first detector column (which affects the first two data points in the figure), there is a flux variation of up to 15% from column to column. (2) This column-to-column variation has only a weak dependence on wavelength. The cause for this residual is not quite clear at this point. As a first-order empirical correction to the IC residual, we have derived a correction factor per detector column in Table 4.2 from averaging a number of mapping observations similar to that of Arp 231. Dividing Table 4.2 into the observed IC image in a column-wise way leads to our composite IC that reduces the residual flux variation to about 5% in Fig. 4 (except for the first detector column) and brings the flux measured between the two default dither positions into reasonable agreement for the observed calibration stars. This composite IC is used in the pipeline starting S15(?).

Table 1. Some Important Post-BCD Files for MIPS/SED

Abbreviation	File contents
_maic.fits _munc.fits _mosst.fits	Mosaic difference image and its associated uncertainty and std images.
_sed.tbl	ASCII table containing the extracted 1-d spectrum
_maicn.fits _muncn.fits _mcovn.fits _mossn.fits	Mosaic ON image and its associated uncertainty, coverage and std images.
_maicf.fits _muncf.fits _mcovf.fits _mossf.fits	Mosaic OFF image and its associated uncertainty, coverage and std images.

Table 2. Column-wise Correction Factors to IC

Det. Col.	Correction	Det. Col.	Correction
1	0.529	9	1.008
2	1.102	10	1.082
3	0.995	11	1.026
4	1.099	12	1.052
5	0.938	13	0.958
6	0.919	14	1.045
7	0.956	15	1.098
8	0.948	16	1.005

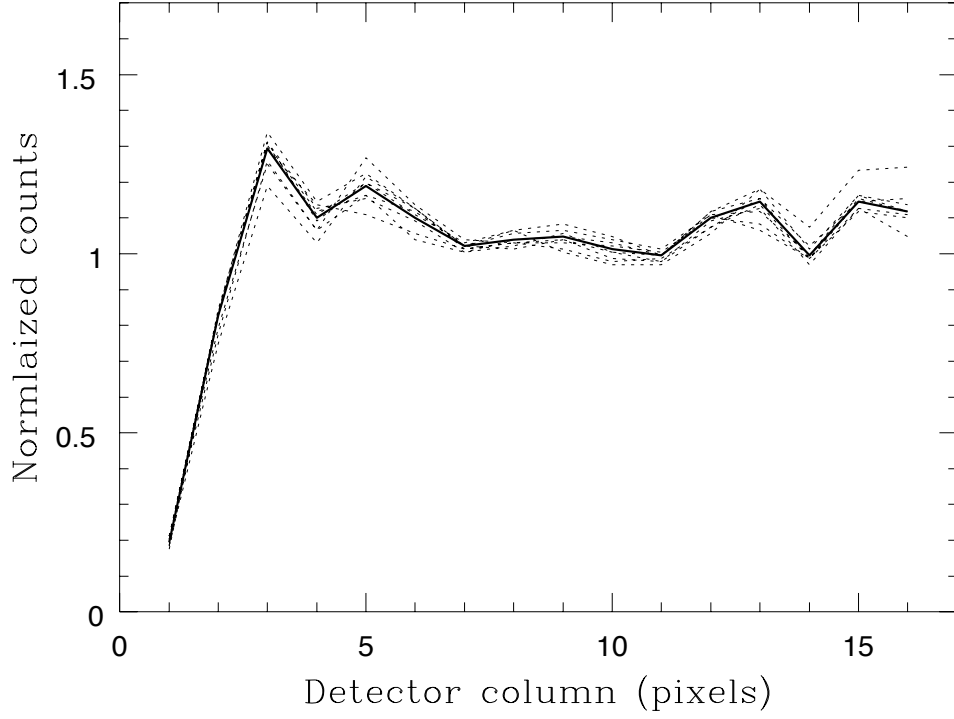


Fig. 3.— Plot of the average spatial profile (dotted lines) over detector rows 9-15 for each of the 9 IC observations acquired between MIPS campaigns 20 and 24. The thick solid curve shows the median result from these 9 IC observations.

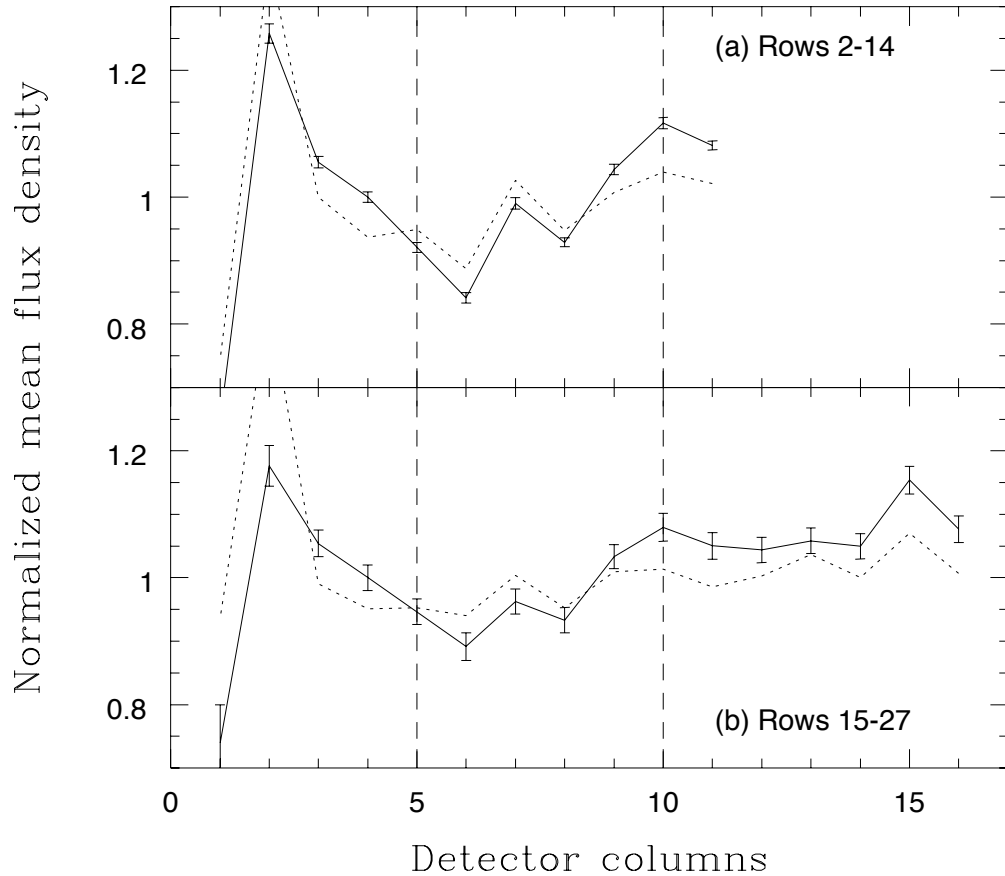


Fig. 4.— Plots (in solid lines) of the average flux of a spectrum extracted within a 3-column aperture at each of the 16 pointings of the mapping observation of Arp 231 as a function of the spectral location on the detector. (a) is for the average over detector rows 2-14 and (b) over rows 15-27. Each data set has been normalized so that its mean is close to unity. A simple column-wise self correction (see the text) brings each solid curve to the dotted one. The two dashed vertical lines indicate the default dither positions. Note that the first two flux points in each plot are affected by the first detector column, which is much noisier than the other columns.

4.3. Wavelength Calibration

The dispersion solution was determined in the early phase of the mission by observing a number of bright planetary nebulae and H II regions. The main spectral lines for this purpose are [N III]57.330 μm and [O III]88.356 μm , which have high equivalent widths in these objects. As an example, Fig. 5 illustrates the observed line profiles of the planetary nebula NGC 6543.

The measured line peak positions along with the assumption of a uniform dispersion across the entire wavelength range yields to scale of 1.71 μm per pixel. The first row of the array (i.e., the blue end) corresponds to 52.55 μm . Each line fitting uses 4 independent data points, the wavelength calibration uncertainty is estimated to be on the order of 0.4 μm ($\approx 0.5 * 1.71 \mu\text{m} / \sqrt{4}$) if the uniform dispersion assumption holds.

This dispersion solution is monitored from time to time during the routine mission. The spectrograph appears to be stable as our wavelength repeatability is better than 0.2 μm between the *Spitzer* In-Orbit Checkout phase by the end of 2003 and the measurements in MC20.

The effective wavelength coverage over detector rows 1-27 of the SED mode is roughly from 51.7 to 97.8 μm . The remaining 5 detector rows at wavelength $> 97.8 \mu\text{m}$ are contaminated by shorter wavelength, second-order light and therefore are not calibrated.

4.4. Aperture Correction

Fig. 6 shows a comparison at 70 μm between the observed mean spatial profile, obtained from the averaged mosaic image of 9 observations of bright stars through MIPS campaign 24 (see the next section for a description of the calibration stars), and the point spread function (PSF) predicted by the *Spitzer* TinyTim model (Krist 200X). The observed profile is the average of the profiles on either side of the peak. The PSF is not well sampled as the two default dither positions are separated by about 5 detector columns. We applied a boxcar smoothing of width D (in units of the detector pixel size) to the model PSF. Clearly, the lower limit for D is 1. The smoothed model results with D = 1, 1.3 and 1.7 are shown in the figure by the solid, dotted and dashed curves, respectively. The inserted log-log plot is to show the outer parts of the profile. All the data sets have been normalized at 9.80'' in radius.

At small radii, the measurements appear to agree well with the model curve of D = 1 although our still sparse sampling rate can not robustly rule out the case of D= 1.3 at this

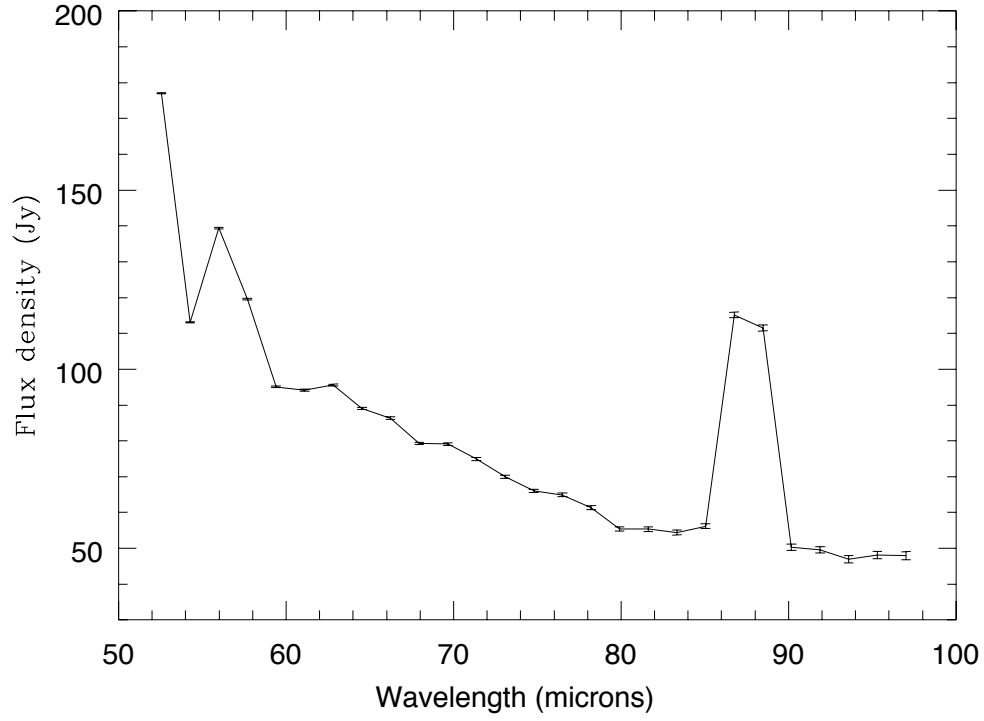


Fig. 5.— An SED spectrum of the bright planetary nebula NGC 6543 from an observation in MIPS Campaign 20. The spectrum is extracted with a 5-column aperture. Both [N III]57 μm and [O III]88 μm , lines are clearly detected.

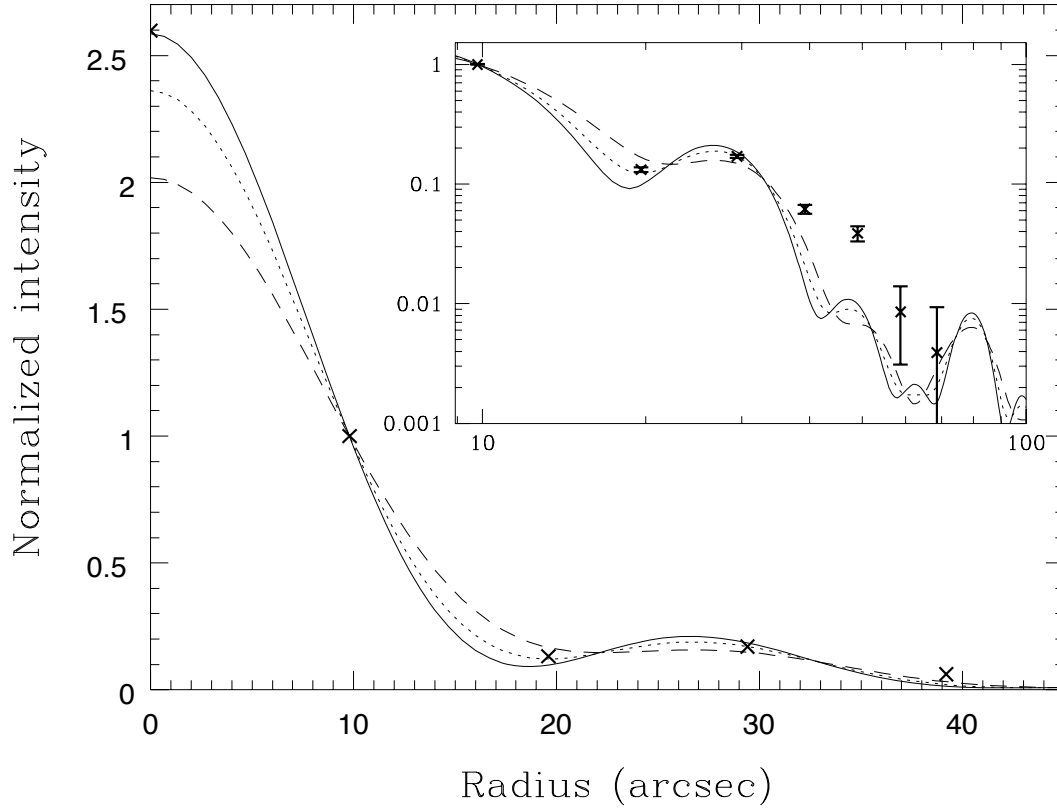


Fig. 6.— Comparison of the observed spatial profile (shown as crosses) with the model predictions at $70\ \mu\text{m}$, which are shown after being smoothed by a boxcar of width of $D = 1.0$ (solid lines), 1.3 (dotted lines) or 1.7 (dashed lines) times the detector pixel size of $9.80''$. The inserted log-log plot zooms in at outer radii. Statistical error bars are shown only in the log-log insert as they are insignificant at small radii.

point. At large radii ($> 50''$), the observed profile appears to be broader than the model predictions. It is expected to see some “excess” flux at faint flux levels due to a possible flux nonlinearity effect (see §5), but the observed excess seems to be too great to be counted for by this effect. Further investigation is needed to see if it is from cirrus emission around some of the calibration stars.

Table 4.4 tabulates the aperture corrections using the model with $D = 1.0$ for both aperture sizes of 5 and 3 columns. The difference in aperture corrections between $D = 1.0$ and $D = 1.3$ is less than 2% at any wavelength. The aperture correction ratio between the two aperture sizes in Table 4.4 can be measured reliably using our bright calibration stars. The comparison of the observed ratios with the model prediction from Table 4.4 indeed favor $D = 1$ with an agreement within 2-3%.

If Fig. 6 implies that the actual PSF has a wing that is roughly twice as bright as what the $D = 1$ model predicts, extended-source flux calibration using the aperture correction factors in Table 4.4 could be off by up to 10%. Note that point-source flux calibration is not affected by this uncertainty.

4.5. Flux Calibrations

4.5.1. Calibration Stars and Spectral Response Function

The primary flux calibrators for the SED mode are bright stars from a list compiled for the flux calibration of the MIPS $70\ \mu\text{m}$ photometric mode. These are mostly supergiants of spectral type K, plus stars of other spectral types (A, G or M). The far-infrared stellar photosphere extrapolations from mid-infrared measurements for these types of stars are described by Rieke et al. (2006) and Engelbracht et al. (2006).

Because the spectral sensitivity of the SED mode decreases fairly steeply as wavelength increases, we have chosen our calibration stars in three flux ranges at $70\ \mu\text{m}$: (1) a few stars brighter than 10 Jy, (2) moderately bright stars of 3-5 Jy, and (3) “faint” stars of ~ 0.5 Jy. Our observation strategy is such that we reach $S/N > 5 - 10$ (except in a couple of early MIPS campaigns) for stars in (1) over the entire wavelength range, for stars in (2) shortward of $\sim 85\ \mu\text{m}$, and for those in (3) shortward of $\sim 70\ \mu\text{m}$. This tiered strategy allows for reasonable integration times at all the three flux levels, and tests on whether there is a significant flux nonlinearity in the detector responsivity.

Table 4.5.1 lists observations of the calibration stars through MIPS campaign 24. The table columns are, from the left to right, the star catalog name, model predicted flux density

Table 3. Aperture Corrections

Detector Row (1)	$\lambda(\mu\text{m})$ (2)	$C_{\text{aper}}(5\text{cols})$ (3)	$C_{\text{aper}}(3\text{cols})$ (4)
1	52.556	1.574	1.748
2	54.266	1.600	1.770
3	55.976	1.626	1.793
4	57.686	1.652	1.815
5	59.395	1.678	1.837
6	61.106	1.706	1.860
7	62.816	1.735	1.882
8	64.525	1.763	1.905
9	66.236	1.792	1.927
10	67.946	1.821	1.950
11	69.656	1.850	1.972
12	71.365	1.878	2.000
13	73.076	1.905	2.028
14	74.785	1.933	2.056
15	76.495	1.960	2.084
16	78.206	1.987	2.112
17	79.916	2.015	2.141
18	81.626	2.040	2.175
19	83.335	2.065	2.210
20	85.046	2.090	2.245
21	86.756	2.115	2.280
22	88.465	2.140	2.315
23	90.175	2.166	2.350
24	91.886	2.191	2.392
25	93.596	2.216	2.434
26	95.305	2.241	2.476
27	97.016	2.266	2.518

at $71.4\ \mu\text{m}$ (see Rieke et al. 2006), number of cycles used in the observation, MIPS campaign number and the AOR tag in the *Spitzer* archive.

A spectral response function is derived for each observation of a calibration star. This was done on the difference image between the mosaicked on-target frames and the mosaicked off-target frames. An aperture of 5 detector columns was used for a spectrum extraction. The extracted spectrum was then divided into the model spectrum to give rise to the spectral response function in units of Jy per MIPS unit. To use the units of MJy sr^{-1} per MIPS unit, the result is further divided by the detector pixel size of $9.80'' \times 9.80''$. Note that the spectral response function derived in this way includes the spectral signature of the diffuse Galactic emission via the IC used in the data reduction. Thus, the spectral response function *changes* if a *different* IC is used in the data reduction. This IC signature is removed from the data since the same spectral response function is applied to all SED-mode targets, including calibration stars.

Fig. 7 is a plot of the resulting spectral response functions from the bright calibration stars. The r.m.s. scatter among the individual response measurements is 5% or less at all wavelengths. Table 4.5.1 is the mean spectral response function derived from the data shown in Fig. 7 using the IC image that had been normalized by its median within the image section [2:16,1:31]. The quoted uncertainty [Column (4)] is the sample standard deviation of the mean, with each observation of an equal weight in averaging.

4.5.2. Comparison with Models and Previous Observations

An empirical way to drive an absolute calibration accuracy is to compare SED measured fluxes with the model predicted values for stars not used in the derivation of the spectral response function. This is shown in Fig. 8 at three representative wavelengths: 60, 71.4 and $80\ \mu\text{m}$. From these data, it is reasonable to conclude that a flux accuracy better than 10% is achieved down to a flux density of $\sim 0.5\ \text{Jy}$ at the blue end of the spectra, or a couple of Janskys near the red end. This empirical accuracy estimate includes uncertainties in the stellar model fluxes.

In Fig. 8 the faint stars apparently have a lower spectral response than the bright stars. This is most noticeable at $60\ \mu\text{m}$, at which the difference is on the order of 5-7% over the $70\ \mu\text{m}$ flux range of 0.5-18 Jy. Since the same detector is used in both the SED and photometry modes, a point-source flux range of 0.5-20 Jy at $70\ \mu\text{m}$ in the SED mode provides equal amount of in-band power as a point source of $2 \times 0.1 \times (0.5 - 20)$ Jy or 0.1-4 Jy in the $70\ \mu\text{m}$ photometry mode, where the factor of 2 accounts for the SED aperture effect

Table 4. Observing Log of SED Calibration Stars

Star (1)	Sp. Type (2)	$f_v(71.4)$ (3)	N_c (4)	MC (5)	AOR (6)
HD100029	M0III	1.11	3	5	9190144
HD131873	K4III	3.14	3	5	9190656
HD045348	F0II	3.30	3	6	9456640
HD048915	A0V	2.74	3	6	9457152
HD082668	K5III	1.52	6	7	9655552
HD211416	K3III	1.14	6	7	9657856
HD124897	K1.5III	14.7	6	10	11625216
HD018884	M1.5III	4.63	6	18	13124352
HD045348	F0II	3.30	9	18	13124608
HD091056	M0III	0.582	12	18	13124864
HD108903	M3.5III	18.8	6	18	13123840
HD120477	K5.5III	0.640	12	18	13125120
HD124897	K1.5III	14.7	6	18	13124096
HD029139	K5III	13.1	6	19	13309440
HD045348	F0II	3.30	9	19	13309952
HD051799	M1III	0.594	12	19	13310208
HD091056	M0III	0.582	12	19	13310464
HD108903	M3.5III	18.8	6	19	13309184
HD164058	K5III	3.13	9	19	13309696
HD060522	M0III	0.754	12	20	13440256
HD062509	K0IIIb	2.40	9	20	13440000
HD070272	K4.5III	0.554	12	20	13440512
HD150798	K2II-III	2.76	9	20	13439744
HD164058	K5III	3.13	9	20	13439232
HD045348	F0II	3.30	9	21	13615872
HD081797	K3II-III	2.70	9	21	13616384
HD082308	K5III	0.51	12	21	13616640
HD131873	K4II	3.14	9	21	13616128
HD164058	K5III	3.13	9	21	13615616
HD198542	M0III	0.80	12	21	13616896
HD108903	M3.5III	18.8	6	22	15248640
HD120477	K5.5III	0.64	15	22	15249408
HD124897	K1.5III	14.7	6	22	15248896
HD137759	K2III	0.48	15	22	15249664
HD164058	K5III	3.13	9	22	15249152
HD091056	M0III	0.582	18	23	15423488
HD108903	M3.5III	18.8	6	23	15422720
HD123123	K2III	0.483	18	23	15423744
HD124897	K1.5III	14.7	6	23	15422976
HD164058	K5III	3.13	9	23	15423232
HD006860	M0III	5.47	9	24	15811840

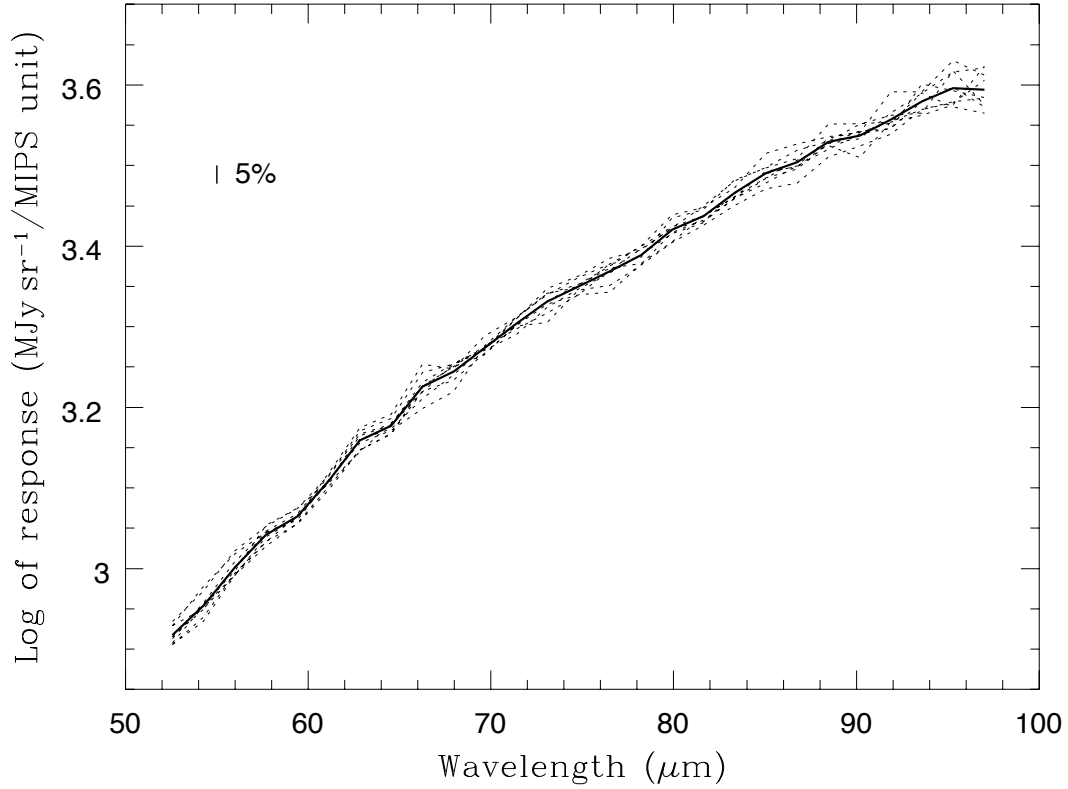


Fig. 7.— Spectral response functions (dotted lines) for a 5-column aperture spectrum extraction, derived independently from 9 observations of 3 bright stars: HD124897 (spectral type K1.5III, 14.7Jy at $70\mu\text{m}$; 4 observations shown here), HD108903 (M3.5III, 18.8Jy; 4 observations), and HD029139 (K5III, 13.1Jy; 1 observation). The thick solid line is the mean response after assigning an equal weight to each individual measurement. A 5% error bar is shown for comparison.

Table 5. Mean Spectral Response Function

Det. Row (1)	$\lambda(\mu\text{m})$ (2)	Resp. ^a (3)	σ_{mean}^b (4)
1	52.556	13737	115
2	54.266	15210	161
3	55.976	17247	155
4	57.686	19221	133
5	59.395	20573	111
6	61.106	23149	120
7	62.816	26419	226
8	64.525	27963	178
9	66.236	31741	398
10	67.946	33667	301
11	69.656	36524	188
12	71.365	39683	225
13	73.076	42841	444
14	74.785	45351	289
15	76.495	48034	490
16	78.206	50939	378
17	79.916	55518	495
18	81.626	58381	396
19	83.335	63134	522
20	85.046	67530	665
21	86.756	70506	758
22	88.465	75588	653
23	90.175	77918	781
24	91.886	82470	996
25	93.596	87878	936
26	95.305	92194	1522
27	97.016	92780	1582

^aMean spectral response in units of MJy sr⁻¹ per MIPS unit.

^bSample standard deviation of the mean spectral response.

Table 6. Timeline of MIPS/SED IPP File Updates

Campaign No. (1)	+1' chop (2)	+2' chop (3)	+3' chop (4)	−1' chop (5)
Pre-MC19	None	None	None	None
MC19	None	None	Updated	None
MC21	None	Updated	Updated	Updated
MC23	None	Updated	Updated	Updated
Post MC23	None	None	None	None

Table 7. Estimated Pointing Offsets^a

Campaign No. (1)	+1' chop (2)	+2' chop (3)	+3' chop (4)	−1' chop (5)
MC19 or earlier	0.0''	+1.2''	+2.4''	+2.5''
MC21 and MC22	0.0''	+2.6''	+4.8''	+5.3''
MC23 or after	0.0''	+0.8''(b)	+0.6''(b)	+0.0''

^aA positive offset is defined to be in the direction of increasing detector row.

^bThese offsets should be acceptable because the pointing jitter from the scan mirror could be as large as 1''.

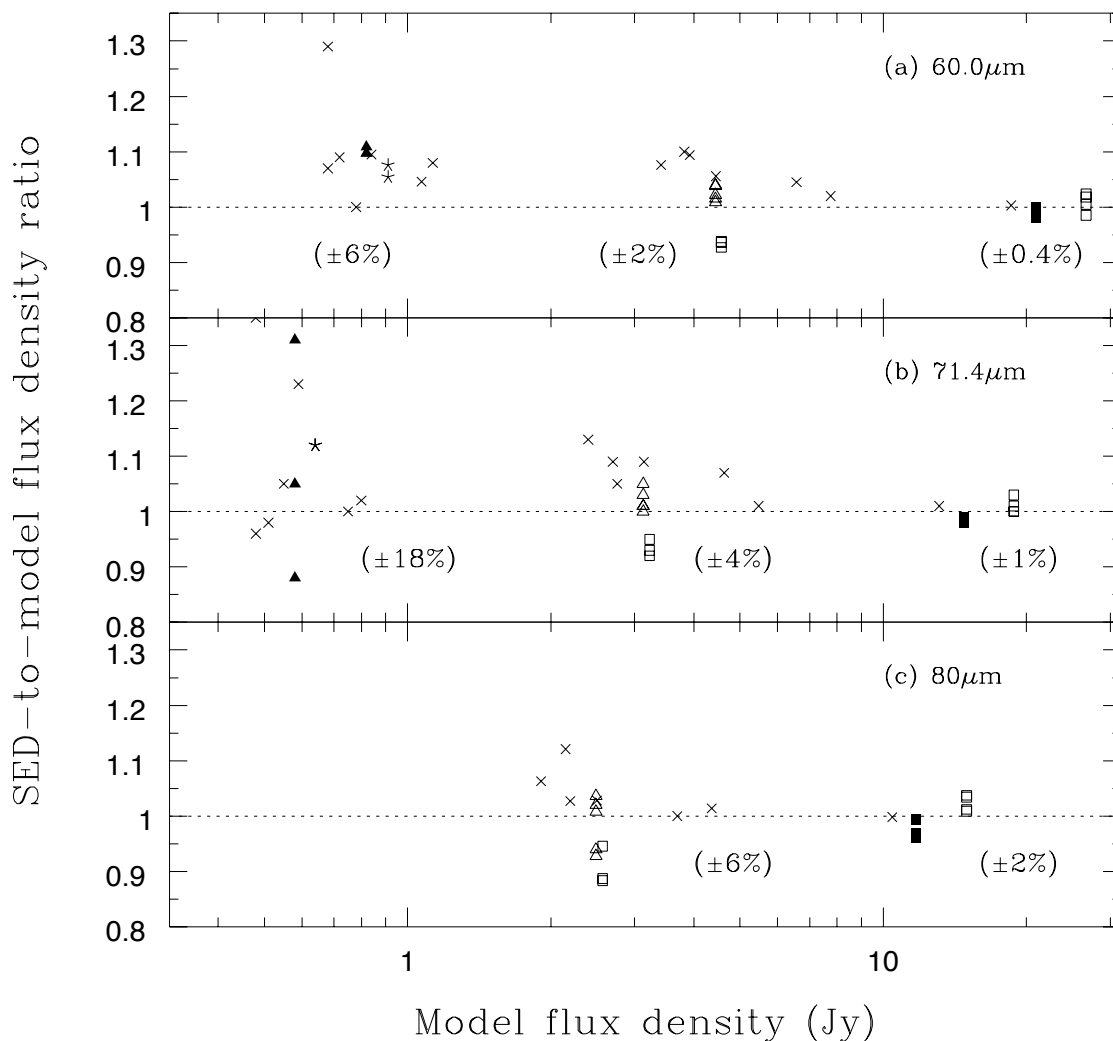


Fig. 8.— The ratio of the measured-to-predicted flux densities for SED calibration stars at (a) $60\ \mu\text{m}$, (b) $71.4\ \mu\text{m}$, and (c) $80\ \mu\text{m}$, as a function of the predicted $71.4\ \mu\text{m}$ flux density. Stars observed in multiple campaigns are distinguished by different symbols to indicate the degree of measurement repeatability; those stars observed only once are each represented by a cross. The number in a pair of brackets indicates the typical statistical uncertainty for a measurement in the group of stars of comparable fluxes.

and the factor 0.1 for the effective difference in bandwidth. The flux calibration of the $70\ \mu\text{m}$ photometric mode is mainly based on standard stars of $71.4\ \mu\text{m}$ flux densities between 0.1-3 Jy, over which no significant flux nonlinearity has been seen in the detector responsivity (see Gordon et al. 2006). Since our bright SED calibration stars are at or slightly above the upper flux threshold, and since stars are brighter at $60\ \mu\text{m}$ than at $71.4\ \mu\text{m}$, it is plausible that part of the apparent flux dependency seen in Fig. 8a can be attributed to the flux nonlinearity.

A number of calibration stars have been observed in multiple campaigns. These include stars of all three flux levels (cf. Fig. 8). The results indicate a fairly high flux repeatability in time: the r.m.s. difference of $\sim 2\%$ near the blue end of the spectrograph to better than 5% near the red end.

A number of the SED calibration stars also have photometric fluxes from the MIPS $70\ \mu\text{m}$ photometry mode, for which the effective wavelength is $71.4\ \mu\text{m}$. For stars, the color correction is negligible in converting the MIPS broad-band flux density to the monochromatic flux density at $71.4\ \mu\text{m}$. Fig. 9 compares the two independent measurements for the 4 stars in common. We limit to our faint calibration stars only as all our bright calibration stars and most of our medium-bright stars are at or above the main flux range (0.1 – 3 Jy) used for the flux calibration of the $70\ \mu\text{m}$ photometry mode. The mean ratio in Fig. 9 is 1.06, which is within the 10% flux uncertainty estimate.

Additional flux comparisons were made with *IRAS* measurements and *ISO* LWS data. Fig. 10 shows such a comparison with *IRAS* 60 and $100\ \mu\text{m}$ fluxes for the galaxy NGC 4418, and with *ISOLWS* data for the galaxy Mrk 231. The results from these cross-comparison analyses are all consistent with our conclusion that the absolute flux calibration of the SED mode is accurate to 10% or better for point sources.

Table 8. Error Budget for Flux Calibration of Extended Sources

Error Source	Estimated Error
Point-source flux uncertainty	$\leq 10\%$
Residual IC uncertainty:	$\sim 5\%$
Aperture correction uncertainty	$\leq 10\%$
Total:	$\sim 15\%$

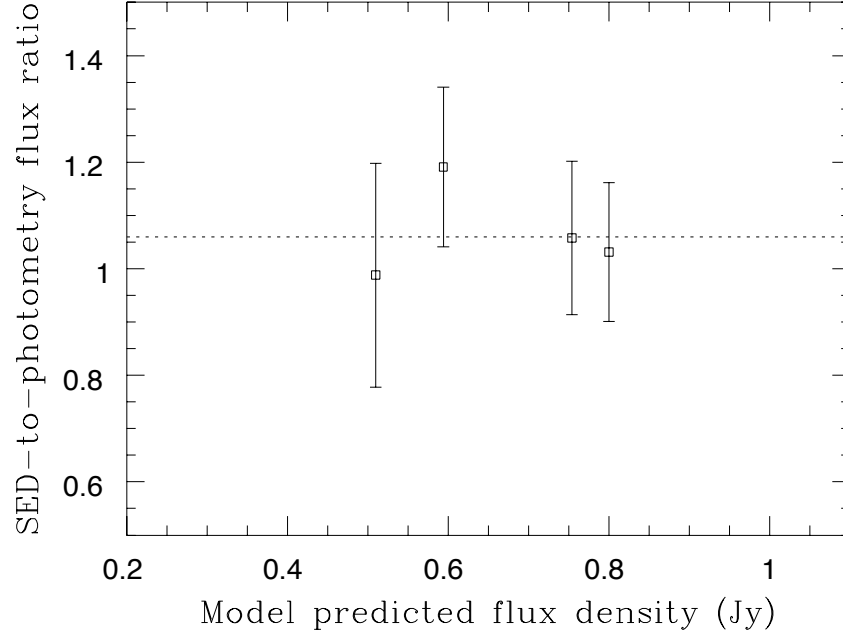


Fig. 9.— Plot of the observed SED-to-photometric flux density ratios as a function of the model-predicted flux density at $71.4\mu\text{m}$ for a subset of our faint calibration stars with available MIPS $70\mu\text{m}$ photometric fluxes. The error bars shown are SED statistical uncertainty only. The dotted line indicates the mean ratio.

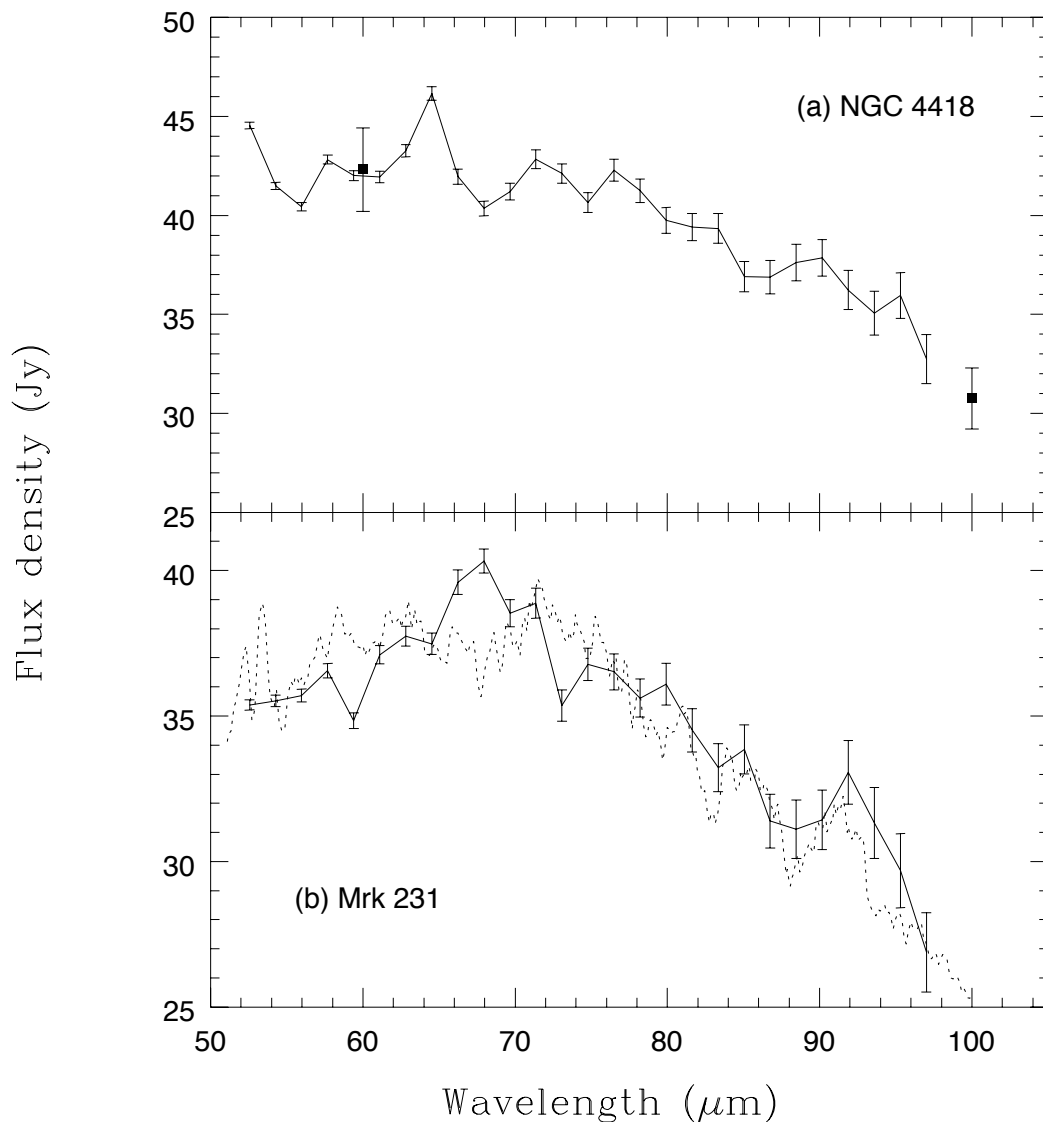


Fig. 10.— Comparisons of SED fluxes (as a solid line) with *IRAS* 60 and 100 μm fluxes for the galaxy NGC 4418 in (a), and with an ISO-LWS spectrum (dotted line) from *ISO* archive (TDT = 18001306) for the galaxy Mrk 231 in (b). The *IRAS* data, taken from Soifer et al. (1989), are assigned with an 5% error bar here. The LWS data have been cleaned up and smoothed with a box car of 7 ISO-LWS pixels in width.

4.5.3. Pointing Offsets and Flux Systematics in some Campaigns

It became noticed that the targets are slightly off the slit center line in early campaigns for chop throws other than the +1'one. There had been a few updates in the IPP files to those parameters controlling the chop throw-related pointing in the SED mode. As a result, for a given chop throw, its typical pointing offsets (from the center line of the slit) may be different in different campaigns.

Table 4.5.1 below shows in which campaign a pointing adjustment was made. The corresponding measured pointing offsets are given in Table 4.5.1. Since the SED flux calibration is carried out with the +1' chop throw where little pointing offset has been seen, the calibrated flux of a point source is underestimated by a small percentage in the campaigns where the selected chop throw has a non-zero pointing offset in Table 4.5.1. This flux underestimate is on the order of -5% (-10%) for an offset of $\pm 2.4''$ ($\pm 4.8''$).

4.5.4. Extended Source Fluxes

Since the SED flux calibration is based on stars, both aperture correction uncertainty and the illumination residual effect have little impact on the flux of a point-source observation. However, they do introduce some additional uncertainties to the surface brightness calibration of an extended source. Table 4.5.1 summarizes the error budget for the case of extended sources, in which the total flux uncertainty is estimated to be on the order of 15% at this point.

The galaxy merger system Arp 299 was mapped by a 4x1 raster map (AOR = 12919296) in the MIPS SED mode. The map centers at R.A. = $11^h 28^m 32.3^s$ and Dec = $58^\circ 33' 43''$ with the SED slit oriented at about 119° (N to E). With a raster step size equal to the width of the SED slit, the map covers the whole system (in optical) with no spatial gap. Fig. 11 compares an *ISO* LWS spectrum (TDT = 18001306) of Arp 299 with our spatially integrated SED spectrum within a rectangular aperture of $78.4'' \times 88.2''$. This aperture size is slightly larger than the circular LWS beam whose diameter ranges from $84.6''$ to $77.2''$ over $50\text{-}100\ \mu\text{m}$ (cf. Table 5.9 of Gry et al. 2003). Both data sets are based on their respective extended-source flux calibration. Since Arp 299 is only mildly extended with respect to the LWS beam, the extended-source flux calibration may somewhat underestimate the LWS flux. This, together with the fact that a larger aperture is our SED data, may be more than adequate to explain the difference in flux in Fig. 11. Regardless of this, the overall agreement is still better than 15% cited in Table 4.5.1.

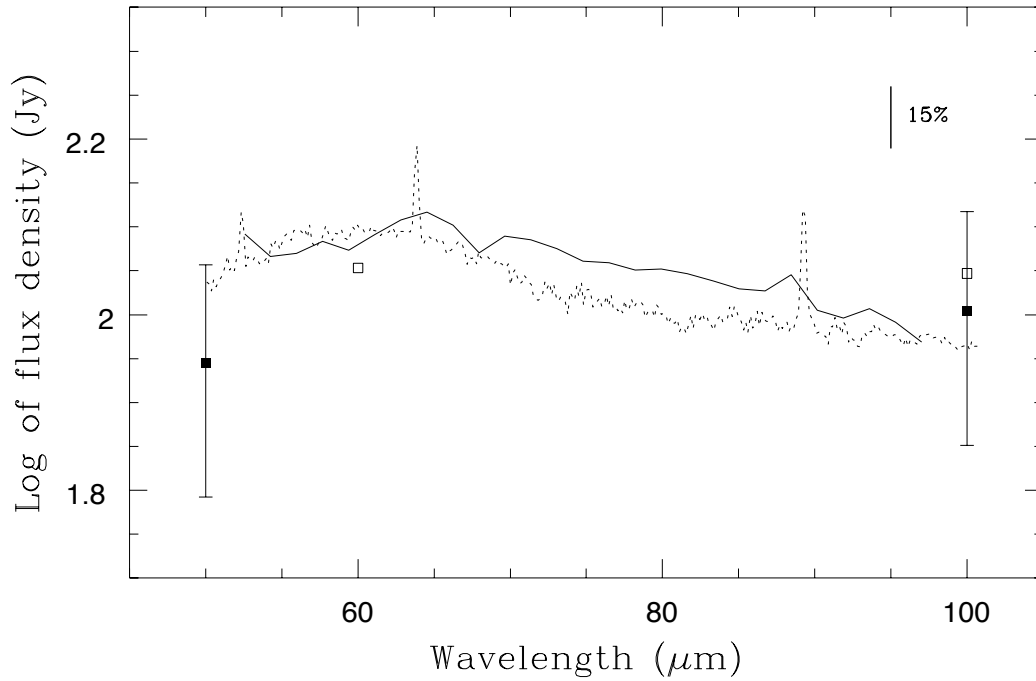


Fig. 11.— Comparison of the spatially integrated SED spectrum (solid line) with *ISO* LWS result (dotted line) for the extended galaxy system Arp 299. The aperture used for extracting the SED spectrum is $78.4'' \times 88.2''$, which is somewhat larger than the circular LWS beam of a diameter of $84.6''$ to $77.2''$ over $50\text{-}100\ \mu\text{m}$ (cf. Table 5.9 of Gry et al. 2003). The LWS spectrum is based on the extended source flux calibration (cf. Table 5.10 of Gry et al. 2003). Also shown are *IRAS* measurements from Sanders et al. (2003; open squares) and Joy et al. (1989; solid squares).

4.5.5. *Remarks on Flux Nonlinearity*

MIPS Ge detector flux nonlinearity will be fully addressed using calibration data taken in the $70\mu\text{m}$ imaging mode, which is more sensitive than the SED mode. No significant (i.e., $\lesssim 10\%$) flux nonlinearity is seen in the SED mode over a flux range of 0.5 to $\sim 40\text{ Jy}$ at $70\mu\text{m}$. However, for a flux far away from this range, the flux nonlinearity could be increasingly important. Without a proper correction for it, the systematic effect from a flux nonlinearity would be an underestimate (overestimate) of the real flux of a *very* bright (faint) source.

REFERENCES

- Engelbracht, C. W., et al. 2006 (in preparation).
- Gorden, K. D., et al. 2005, PASP, 117, 503.
- Gorden, K. D., et al. 2006 (in preparation).
- Gry, C., et al. 2003, LWS – The Long Wavelength Spectrometer, ESA publication.
- Joy, M., Lester, D. F., Harvey, P. M., Telesco, C. M., Decher, R., Rickard, L. J., & Bushouse, H. 1989, ApJ, 339, 100.
- Krist, J. 200X, Spitzer TinyTim User’s Guide.
- Rieke, G. H., et al. 2006 (in preparation).
- Sanders, D. B., Mazzarella, J. M., Kim, D. C., Surace, J. A., & Soifer, B. T. 2003, AJ, 126, 1607.
- Soifer, B. T., Boehmer, L., Neugebauer, G., & Sanders, D. B. 1989, AJ, 98, 766.